Applied Surface Science 527 (2020) 146688

Contents lists available at ScienceDirect

Applied Surface Science

journal homepage: www.elsevier.com/locate/apsusc

Quantitative correlations between photochemical performance and low-electron-density defect

Huan Liu[a], Xiaofeng Yin[b], Huiru Cheng[c], Xiaoning Li[d], Yingying Zhang[a], Wen Gu[a], Wei Zou[a], Liuyang Zhu[a], Qingmei Wu[a], Haoliang Huang[d], Jianlin Wang[d], Bangjiao Ye[c], Zhengping Fu[a,e,*], Yalin Lu[a,d,e,*]

[a] Department of Materials Science and Engineering, CAS Key Laboratory of Materials for Energy Degradation, University of Science and Technology of China, Hefei 230026, PR China
[b] Henan Collaborative Innovation Center of Energy-Saving Building Materials, Xinyang Normal University, Xinyang 464000, China
[c] State Key Laboratory of Particle Detection and Electronics, University of Science and Technology of China, Hefei 230026, PR China
[d] Anhui Laboratory of Advanced Photon Science and Technology, National Synchrotron Radiation Laboratory, University of Science and Technology of China, Hefei 230026, PR China
[e] Synergetic Innovation Center of Quantum Information and Quantum Physics & Hefei National Laboratory for Physical Sciences at Microscale, University of Science and Technology of China, Hefei 230026, PR China

ARTICLE INFO

Keywords:
Photochemistry
Defect
Photocatalysis
Quantitative correlation

ABSTRACT

Establishing definite correlations between specific defects and physicochemical processes is the prerequisite for applying defect-engineering to optimize material properties. However, systematic investigations are required to fulfill this task. In this work, for the first time, a kind of defect with low electron density is quantitatively demonstrated to be correlative with photocatalysis efficiency by using perovskite oxide $Na_{0.5}Bi_{2.5}Ta_2O_9$ nanosheets as the model material, in which the defect was systematically introduced and engineered. More importantly, the correlation is found to be not only valid for photocatalysis in $Na_{0.5}Bi_{2.5}Ta_2O_9$, but also is pervasive in various materials and different photochemical processes, though it has been overlooked in previous reports. The defect with low electron density acts as the recombination center for photogenerated carriers, therefore it is detrimental to the photo(electro)chemical performance, and the elimination of this kind of defect will be critical for improving photochemical efficiency.

1. Introduction

The physicochemical properties are tightly related to internal defects and electronic structures in catalysts due to the following reasons. First, defects can form defective energy levels and adjust the bandgap to extend the photo-responsive range [1–3]. Second, the presence of surface defects can provide coordinatively unsaturated states which alter surface charge density distribution and serve as reactive sites [4]. Third, defects can change the crystal structures and affect the behaviors of photogenerated electrons and holes [5]. Therefore, defect engineering has been a widely used strategy to optimize the physicochemical properties of catalysts and has become a hot research field.

Positron annihilation spectra (PAS) can provide valuable information about the electronic and physical structures of defects. The lifetime of positrons in PAS is inversely proportional to the local electron density of defects because defects can trap positrons and the low electron density reduces the positron annihilation rate, leading to an increase of the lifetime. Therefore, it can give information about both size and type of defects, while the relative intensity (I) can reflect the concentration and distribution of defects [1,6]. In nanoparticles, positron annihilation spectra can be fitted with three components with the lifetime of τ_1, τ_2 and τ_3 ($\tau_1 < \tau_2 < \tau_3$), respectively [6–12]. As depicted in Fig. 1, the component with lifetime τ_1 is usually ascribed to small vacancies like mono-vacancies or shallow positron traps like oxygen vacancies [6,7,12,13], and the second component with lifetime τ_2 is commonly due to positrons trapped by larger size defects such as oxygen vacancy clusters on the surface [8,14]. The component with the longest lifetime τ_3 is frequently related to the annihilation of *ortho*-positronium (*o*-Ps, the bound state formed by a positron with an electron) formed at the large size defect with low electron density, such as void in the materials [10,11,15–17]. Therefore, defects related to τ_3 is marked as low-electron-density defects [11,16].

* Corresponding authors.
E-mail addresses: fuzp@ustc.edu.cn (Z. Fu), yllu@ustc.edu.cn (Y. Lu).

https://doi.org/10.1016/j.apsusc.2020.146688
Received 29 March 2020; Received in revised form 10 May 2020; Accepted 12 May 2020
Available online 20 May 2020

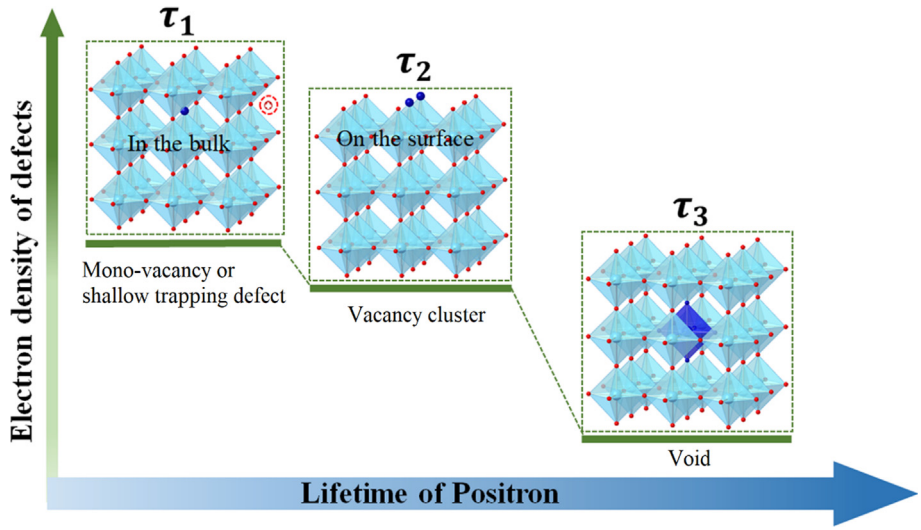

Fig. 1. Schematic illustration of the lifetime of positrons and the different types of defects revealed by positron annihilation spectra (PAS).

Establishing the relationship between various defects and performance is the prerequisite to effectively apply the defect-engineering strategy. To date, there are many reports about the correlation between photoelectrochemical performance and defects created by various methods. It was found that the surface electron structure was engineered by oxygen vacancies in {1 1 1} facet of CoO, which can facilitate charge transfer and optimize absorption energies in oxygen reduction/evolution reactions [18]. Zhou et al. developed oxygen-vacancy defect engineering at the Pt/TiO_2 interface to make photooxidation sites close to photoreduction sites, achieving an ultrahigh hydrogen yield per photon of 1.28 [19]. Similarly, the Cu-TiO_2 nanosheets with dominant {0 0 1} facets and surface oxygen vacancy showed an enhanced photocatalytic reduction of CO_2 to CH_4 [20]. Li's group successfully adjusted surface oxygen vacancy clusters to promote the CO oxidation on CeO_2 nanorods, and the oxygen vacancy clusters were proved to be favorable for oxygen migration [8]. Xie et al. introduced Co vacancies in atomic-scale thickness $CoSe_2$ to enhance the electron transfer and the oxygen adsorption rate, which improved the oxygen evolution reaction [9]. Steele's group reported the Bi_2WO_6 monolayers rich stable interior W vacancies had crucial influence on the physical properties and boosted the solar photocatalytic oxidation of benzylic alcohols by 140% [21]. Particularly, Kong et al. studied the concentration ratio of bulk to surface defects in TiO_2, and found that the ratio greatly affected the separation of electron-hole pairs, and therefore affected photocatalytic CO_2 reduction [7]. In these works, they mainly focused on components with τ_1 and τ_2, while the component with τ_3, low-electron-density defect, which was characterized by long positron lifetime in PAS, was also found but was always overlooked because of the low concentration. In fact, defects with low concentration can play a pivotal role in physical or chemical processes. For example, the conductivity and Fermi level change significantly when the doping concentration of single-crystal silicon reaches an only ultralow concentration of 10^{16} cm^{-3}. Therefore, we infer the existence of the relationship between the low-electron-density defect and physicochemical performance by surveying the previous reports. However, a systematic study is urgently required to establish definite correlations.

Due to the unique and tunable structures or electronic properties [22–24], perovskite oxides such as $Sr_2Bi_2Nb_2TiO_{12}$ [3], $HCa_2Nb_2TaO_{10}$ [23], $Bi_7Fe_3Ti_3O_{21}$ [25], Bi_3TiNbO_9 [26], and $Na_{0.5}Bi_{2.5}Ta_2O_9$ [27], have been studied in physicochemistry. Especially, the defects in perovskite oxides can be well-tuned by substituting, therefore, they are suitable platforms to systematically study the defects and their relationship with properties. To study this issue of the low-electron-density defects and the relationship, $Na_{0.5}Bi_{2.5}Ta_{2-x}Ti_xO_{9-\delta}$ was adopted in this work as the model material, which was synthesized with a modified molten salt method and the concentration of defects was modulated by the substitution of Ta^{5+} with low valence Ti^{4+}. For the first time, a correlation between low-electron-density defects and photochemical performance is demonstrated. And the decrease of this kind of defect is important for enhancing photocatalytic performance. The optimized nanosheets exhibit a higher generation rate of superoxide radicals ($\cdot O_2^-$), higher photocatalytic rate, and higher photocurrent. We also analyze the data in previous reports and find that the correlation is pervasive for various materials and different photochemical processes.

2. Experimental

2.1. Sample preparation

Single-crystal nanosheets $Na_{0.5}Bi_{2.5}Ta_{2-x}Ti\text{-}xO_{9-\delta}$ (x = 0, 0.05, 0.1, 0.2) (defined as Ti-0, Ti-0.05, Ti-0.1, and Ti-0.2, respectively) were synthesized via modified molten salt method. All the raw reagents were purchased directly from Sinopharm Chemical Reagent Co., Ltd, and were used without any further purification. In a typical synthesis, the stoichiometric ratio of $Bi(NO_3)_3{\cdot}5H_2O$ and $Ti(OC_4H_9)_4$ were firstly dissolved in 4 M dilute nitric acid and C_2H_5OH, respectively. Whereas the corresponding amount of Ta_2O_5 was ultrasonically dispersed in distilled water, then the above two solutions were added to the 4 M dilute nitric acid to form a mixed solution and the mixed solution was stirred for 30 min. Subsequently, the ammonia solution was dropped into the mixed solution until the pH was approximately 9. The obtained white precursor was repeatedly washed with deionized water and then was dried in an oven overnight at 70 ℃. The dried precursor and mixed molten salt (n_{NaCl}/n_{KCl} = 1:1) with a mass ratio of 1:4 were vigorously grounded in an agate mortar for 30 min, then the mixture was heated to 800 ℃ with a rate of 3 ℃/min in a tube furnace and was calcined in air for one hour. Finally, the mixture was cooled to room temperature and washed with deionized water several times and then was dried overnight at 70 ℃.

2.2. Sample characterization

The crystal structures of samples were studied by X-ray diffraction (XRD, Rigaku-TTR III) with Cu Kα radiation (1.5406 Å). The scanning electron microscopy (SEM) was taken on a JSM-6700F instrument. The transmission electron microscopy (TEM), high-resolution transmission electron microscopy (HRTEM), and mapping images were performed on

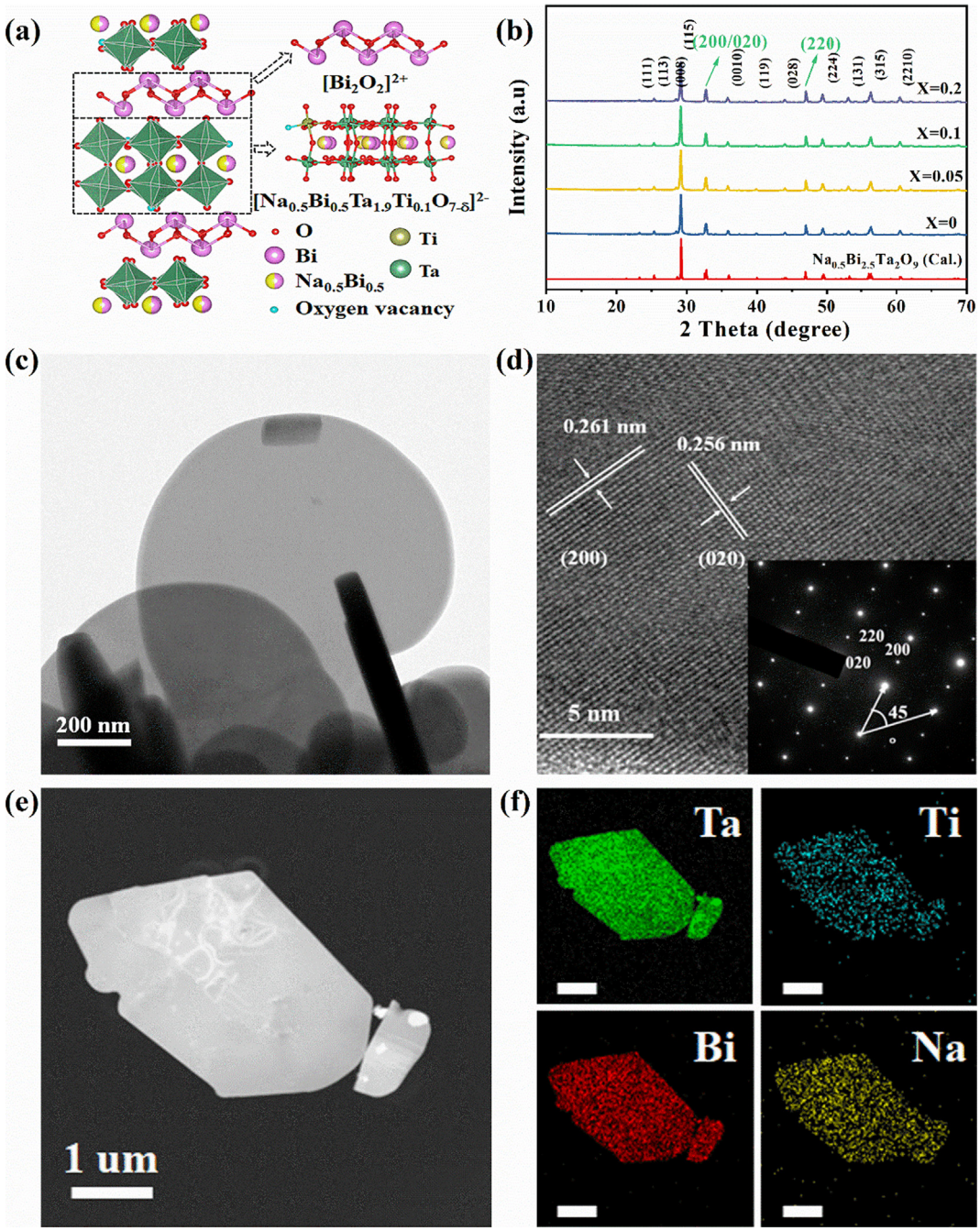

Fig. 2. Structure and morphology characterization for defective Ti-0.1 nanosheets. (a) Crystal structure diagram of Ti-0.1 and schematic illustrating the location of oxygen vacancies in lattice. (b) XRD patterns for as-prepared Ti-*x* samples. (c) TEM images. (d) HRTEM image. And the inset is the SAED pattern. (e–f) STEM image and corresponding EDS element mapping images of Ti-0.1. Scale bars: 1 μm.

a JEM-2010 transmission electron microscope at an acceleration voltage of 200 kV. The Ultraviolet − visible (UV − vis) spectrophotometry was studied on a SOLID 3700 instrument. The soft X-ray absorption spectra (XAS) were collected at the BL10B of the National Synchrotron Radiation Laboratory (NSRL, Hefei, P. R. China). X-ray photoelectron spectroscopy (XPS) measurement was carried out using an ESCALAB 250 X-ray photoelectron spectrometer with Al-Kα irradiation. The specific surface area of the powder samples was characterized by Tristar II-3020 M analyzer. The decay time spectra were monitored by an FLS920 spectrophotometer and the photoluminescence (PL) spectra and Raman spectra were recorded by an F-4600 fluorescent spectrophotometer and SPEX-1403 laser Raman spectrometer, respectively.

2.3. Positron annihilation study

Sandwiched samples of Ti-*x* samples / ^{22}Na source / Ti-*x* samples were pressed into a round disc with a thickness of 1 mm and were used for the positron lifetime experiments, which were carried out with a fast-slow coincidence ORTEC system with a time resolution of 230 ps full width at half-maximum. Positron lifetime was extracted using the ATSUP method [28].

2.4. Photocatalytic activity test

Photodegradation of methylene blue (MB) was carried out at room temperature to test photocatalytic activity under the irradiation of a

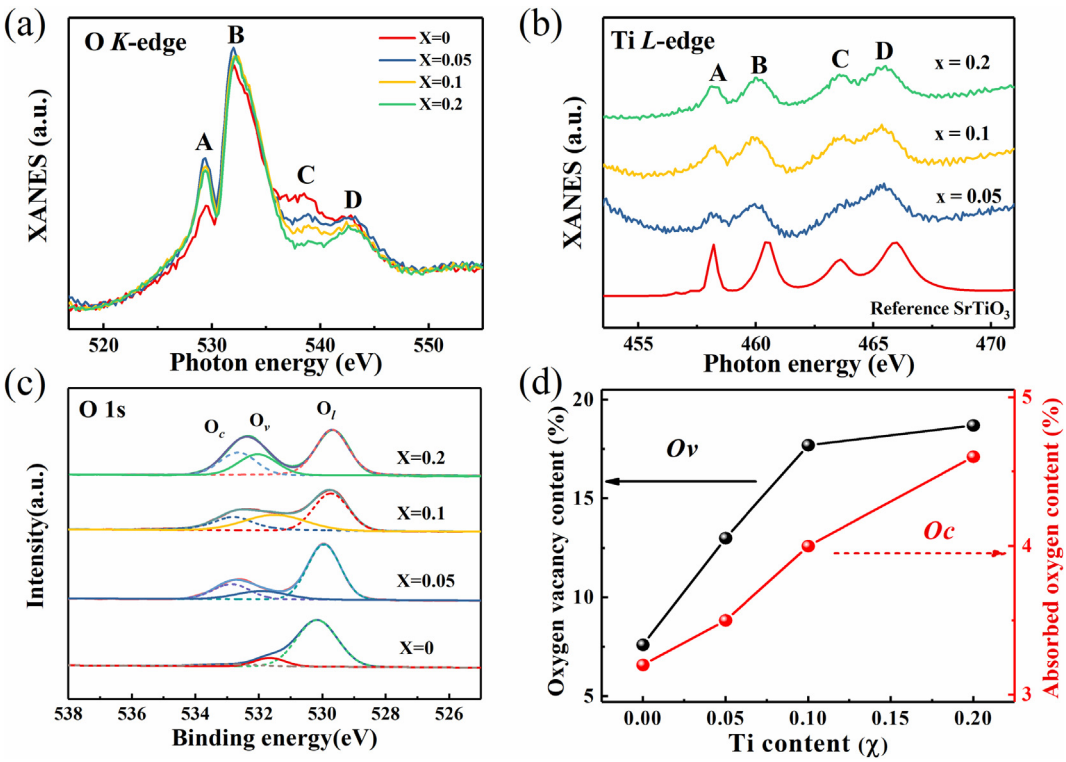

Fig. 3. XAS and XPS spectra for Ti-*x* samples. (a) Normalized O *K*-edge XAS spectra. (b) Normalized Ti *L*-edge XAS spectra. (c) High-resolution O 1 *s* spectra. (d) Content of surface oxygen vacancies (O_V) and chemisorbed oxygen (O_C) in Ti-*x* samples calculated from XPS.

20 W UV lamp with a wavelength of 254 nm. 50 mg photocatalyst was poured into 50 mL MB solution (5 mg L^{-1}) in a 100 mL of the beaker. The suspension was magnetically stirred for 30 min in the dark condition to achieve adsorption–desorption equilibrium, subsequently was exposed to UV light irradiation and 4 mL suspension sample was taken for concentration measurement at regular intervals under continuously stirring. The suspension sample was centrifuged at 10000 rpm to remove the catalyst powders. In addition, the DMPO-assisted (5,5-dimethyl-1-dimethyl N-oxide) electron spin resonance (ESR) signal was used to acquire $\cdot O_2^-$ generated during the photodegradation process. The $\cdot O_2^-$ were detected in a mixed solution consisting of 5 mg powders & 1 mL CH_3OH & 30 μL DMPO.

2.5. Photoelectrochemical measurements

Photoelectrochemical properties were studied in a standard three-electrode cell by a photoelectrochemical system (CHI-660E, Shanghai Chenhua Limited, China). Briefly, 10 mg powder samples were suspended in the mixed colloidal solution formed by 250 μL of isopropanol, 750 μL of deionized water, and 100 μL of membrane solution. The mixed colloidal solution was ultrasonically dispersed to form a uniform solution and then 60 μL of resulting colloidal solution was spin-coated onto the FTO conductive glass and was dried in an oven at 60°C for overnight. The sample powder was tightly fixed on FTO conductive glass by these treatments. FTO conductive glass with powder, Ag/AgCl electrode, and platinum electrode were employed as working electrode, reference electrode and counter electrode, respectively. 0.5 M Na_2SO_4 solution was selected as the electrolyte. For photocurrent test, the curves were collected by switching the Xe lamp light source (PLS-SXE 300, Beijing Perfect Light Science & Technology Co., LTD) (light on and off) every 10 s at the potential of 1 V. Electrochemical impedance spectroscopy (EIS) was carried out at 0.5 V *vs.* Ag/AgCl over a frequency range from 100 kHz to 0.1 Hz. Mott-Schottky (MS) spectra were measured from −1 to 0 V *vs.* Ag/AgCl at a scan rate of 5 mV s^{-1} with a frequency of 1000 Hz, 3000 Hz, and 5000 Hz, respectively.

The charge carrier density (N_d) was calculated according to the Mott-Schottky curves with the following equation: [29]

$$N_d = \frac{2}{e\varepsilon_0\varepsilon} \times \left[\frac{d\left(\frac{1}{C^2}\right)}{dV_s}\right] \tag{1}$$

The electronic charge (*e*) is 1.6 × 10^{-19}C, the vacuum permittivity (ε_0) is taken as 8.86 × 10^{-12}F·m^{-1}, and the relative permittivity (ε) is 102 for $Na_{0.5}Bi_{2.5}Ta_2O_9$ [30]. C (F·cm^{-2}) is the space charge capacitance in the semiconductor (obtained from MS curves), and Vs (V) is the applied potential for MS curves.

3. Results and discussion

The morphologies of $Na_{0.5}Bi_{2.5}Ta_{2-x}Ti_xO_{9-\delta}$ samples are shown in Fig. S1. From the SEM images, the as-prepared samples look like stacked flowers with an average width varying from 200 nm to 2 μm. As clearly displayed in Fig. 2A, the typical Aurivillius-type layered crystal structure of $Na_{0.5}Bi_{2.5}Ta_2O_9$ consisted of alternating layered perovskite slabs $[Na_{0.5}Bi_{0.5}Ta_2O_7]^{2-}$ and fluorite-like $[Bi_2O_2]^{2+}$ units, displaying periodic structure and anisotropy. XRD patterns in Fig. 2B reveal that all the synthesized Ti-doped samples are well indexed to $Na_{0.5}Bi_{2.5}Ta_2O_9$ with the space group A21am, indicating that all the samples are pure phases. The Raman spectrum in Fig. S2 shows that little lattice distortion occurs, because more oxygen vacancies are generated to maintain valence balance when the Ta^{5+} is replaced by Ti^{4+} in $[TaO_6]$ octahedrons. The TEM image of Ti-0.1 sample in Fig. 2C shows the nanosheet morphology. The high-resolution TEM (HRTEM) image of Ti-0.1 nanosheets shown in Fig. 2D. The distances of lattice fringes are 0.261 nm and 0.256 nm, respectively, and the corresponding selected area electron diffraction (SAED) patterns are coincided with the lattice spacing of (2 0 0) and (0 2 0) planes in the XRD patterns of the orthorhombic phase, indicating that the dominantly exposed facet is {0 0 1} facet. Subsequently, the elemental mapping images of Fig. 2E and F reveals that all the elements distribute uniformly on the surface of

{0 0 1} facet of Ti-0.1. Oxygen vacancies should generate in Ti-doped samples to maintain electrostatic balance based on the reaction (Eq. (2)).

$$2Ta_{Ta} + 9O_O \overset{2Ti_{Ti}}{\rightarrow} 2Ti_{Ta}^{'} + V_O^{\cdot\cdot} + 8O_O + \frac{1}{2}O_2 \quad (2)$$

The XAS is applied to characterize the effect of Ti doping due to its good sensitivity to the valence, symmetry, and spin state of the ionic. Fig. 3A and B present the normalized O *K*-edge and Ti *L*-edge XAS of pristine $Na_{0.5}Bi_{2.5}Ta_2O_9$ and Ti-doped samples, respectively. In the O *K*-edge spectra, peak A and B are attributed to the excitation of O 1 *s* electron to the hybridized orbitals of O 2*p*-Ta 5*d*, corresponding to the lower energy t_{2g} and high energy e_g orbitals, respectively. The peaks with higher energy (C, D) arise from the delocalized states derived from the hybridized O 2*p*-Ta 4*sp* states. The intensity of peak A of Ti-doped samples significantly increases because the non-occupied state of Ti 3*d* orbitals is more than that of Ta 5*d* orbitals. However, with the further rise of Ti concentration, the concentration of oxygen vacancy will increase (or in other words, the amount of oxygen atom will decrease). As a result, the intensity of peak A decreases because the number of electrons contributed by oxygen atoms to occupy the Ta 5*d* t_{2g} orbitals and/or the substituted Ti 3*d* t_{2g} orbital becomes less, reducing the transition probability of O 1 *s* to the hybridized Ta 3*d*-O 2*p* bands [31,32]. Meanwhile, the binding energy peak of Ta $4f_{7/2}$ shifts 0.20 eV toward lower binding energy (Fig. S3) [33], indicating a reduction in the oxidation state of Ta. Therefore, the XAS results verify the modulation of oxygen vacancy with Ti doping. The Ti *L*-edge XAS spectrum of Ti-doped samples has four peaks, which is in agreement with the reference sample $SrTiO_3$ results and demonstrates that the oxidation state of Ti in all the doped samples are 4+ [34]. The XPS is applied to reveal the valence information of samples surface. The signal of O 1 *s* in Fig. 3C shows three peaks with the binding energy at about 529.9 eV, 531.1 eV, and 532.5 eV, and these peaks of Ti-doped samples have a slight drift. The lowest binding energy peak is assigned to lattice O (O_L), and higher binding energy peak is ascribed to hydroxyl groups bonded to the metal cations in the oxygen-deficient region (O_V) [35,36], and the highest binding energy peak is attributed to the chemisorbed or dissociated oxygen species from the molecules of water or oxygen (O_C) [35,37]. The XPS spectra of other elements (Na 1 *s*, Bi 4*f*, Ti 2*p*) of samples are shown in Fig. S4. The concentration ratios of surface oxygen vacancies (O_V), chemisorbed oxygen (O_C) are calculated according to the peak areas of O 1 *s* in XPS spectra in Table S1 and Fig. 3D. It can be seen that the concentration of the O_V and O_C monotonically increases when Ti content rises, indicating that the concentration of surface oxygen vacancies increases. The XAS and XPS results verify that the defects in $Na_{0.5}Bi_{2.5}Ta_{2-x}Ti_xO_{9-\delta}$ can be well changed by varying the Ti content, which is in accord with Eq. (2).

The positron annihilation spectrum is a powerful technique to provide direct information about the type and concentration of defects in samples. As shown in Fig. S5 and Table 1, the PAS of Ti-x samples can be well fitted with three components with distinct positron lifetime τ_1, τ_2, and $\tau_3$with relative intensities I_1, I_2, and I_3 [6]. The shortest component (τ_1) is attributed to annihilation of positron as trapped at the small vacancy in the bulk [6,7], and the intermediate one (τ_2) is generally attributed to larger size defects in the materials, such as oxygen vacancy clusters associated on the surface [8,14]. The concentration of the defect with component τ_1 decreases, while that of the defect with component τ_2 increases with the rise of Ti content. This can be ascribed to the aggregation of single oxygen vacancy on surface or to form vacancy clusters with the increase of oxygen vacancy. The concentration trend of component τ_2 is in accordance with Ov trend shown in Fig. 3D. Moreover, as shown in Fig. S6, both τ_1 and τ_2 decrease with the rise of Ti content, which means that the electron density in the materials increases with the incorporation of oxygen vacancy, due to the donor character of oxygen vacancy ($O_O \rightarrow V_O^{\cdot} + e^{'} + \frac{1}{2}O_2 \rightarrow V_O^{\cdot\cdot} + 2e^{'} + \frac{1}{2}O_2$), in agreement with previous reports [38,39]. The longest lifetime component τ_3 may arise from the pick-off annihilation of *ortho*-positronium (*o*-Ps) formed in large voids in the materials [10,11,16]. The lifetime of this kind of defects is relatively longer than that of small defects in bulk and surface (τ_1 and τ_2), respectively. Component with the longest lifetime of τ_3 results from annihilation in regions of lower electron density, thus defects related with τ_3 can be marked as low-electron-density defects [11,16]. In contrast to other components, the lifetime of component τ_3 increases gradually and then decreases with the increase of Ti-doped contents, while the concentration exhibits the opposite tendency. The Ti-0.1 sample has the longest lifetime and lowest concentration of component τ_3, demonstrating that the defects with low-electron-density are not simply surface oxygen vacancies.

The generation of $\cdot O_2^-$ was investigated to study the relationship between physicochemical properties and defects, which is realized via DMPO-assisted ESR technique [40]. As shown in Fig. 4A, there is no signal observed in the dark, while the signal of $\cdot O_2^-$ in all the samples appears after 30 s UV-light irradiation. The nearly 1:1:1:1 quartet pattern indicates that $\cdot O_2^-$ are produced in all the samples under the irradiation, whereas the signal intensity of the Ti-doped sample is higher than that of the undoped sample, revealing that the Ti-doped samples can significantly photo-activate O_2 into $\cdot O_2^-$ species. The ESR signal intensity of$\cdot O_2^-$ is highest in Ti-0.1 sample, meaning the highest generating rate of$\cdot O_2^-$ in Ti-0.1 sample. However, the XPS results have indicated that the concentration of oxygen vacancy and chemisorbed oxygen in Ti-0.1 sample is not the highest, therefore, the surface oxygen vacancy is not the direct factor that determines the generation rate of $\cdot O_2^-$. On the other hand, the above PAS results have disclosed that the positron lifetime of the low-electron-density defect in Ti-0.1 sample is the longest, as well as that the concentration is the lowest. The generating rate of$\cdot O_2^-$ and the positron lifetime τ_3 of low-electron-density defects are depicted in Fig. 4B and Fig. S7, which obviously indicates their correlation. According to the generation reaction of $\cdot O_2^-$: $O_2 + e^- = \cdot O_2^-$, the generating rate of$\cdot O_2^-$ depends on the supply of both O_2 and e^-. Therefore, the ESR results imply that the increase of positron lifetime, along with the decrease of concentration for defects, is beneficial for the transfer of a photogenerated electron to chemisorbed O_2. It is suggested that the low-electron-density defects tend to trap electrons, so the formation of$\cdot O_2^-$ is suppressed, and then physicochemical properties are reduced when the concentration of this kind of defect increases.

To illustrate the transfer efficiency of the photogenerated electron in different samples, the photocurrents were further measured in a 0.5 M Na_2SO_4 electrolyte under 300 W Xe lamp irradiation with several on–off cycles of 10 s interval (Fig. 4C). The current value in the dark is low and the value sharply climbs up to a high level once the light turns on. Ti-0.1 samples again have the highest photocurrent density (6.25 μA/cm^2), which is about 2.2 times higher than that of pristine $Na_{0.5}Bi_{2.5}Ta_2O_9$ (2.93 μA/cm^2). The photocurrent values of different samples are also displayed in Fig. 4B and Fig. S7, which further implies the strong correlation among the electron transfer, generation of $\cdot O_2^-$, and the positron lifetime. The photoluminescence (PL) spectra in Fig. S8 shows that emission band of undoped $Na_{0.5}Bi_{2.5}Ta_2O_9$ sample centers at about 420 nm (2.95 eV), while Ti-doped samples center at about 490 nm (2.5 eV). The energies of PL bands in all samples are far lower than the band gaps determined via UV − vis diffuse reflectance tests in Fig. 4D, therefore the PL should originate from defects [41]. PL decay curves are detected by monitoring the wavelength at 420 nm for

Table 1
Positron Lifetime and Relative Intensities of the Ti-*x* Nanosheets.

Sample	τ_1 (ps)	τ_2 (ps)	τ_3 (ns)	I_1 (%)	I_2 (%)	I_3 (%)
Ti-0	328.2	539.0	2.61	91.8	7.7	0.494
Ti-0.05	260.9	418.0	3.18	76.2	23.3	0.464
Ti-0.1	236.9	382.2	3.50	64.8	35.1	0.077
Ti-0.2	228.0	353.6	3.24	53.6	46.2	0.146

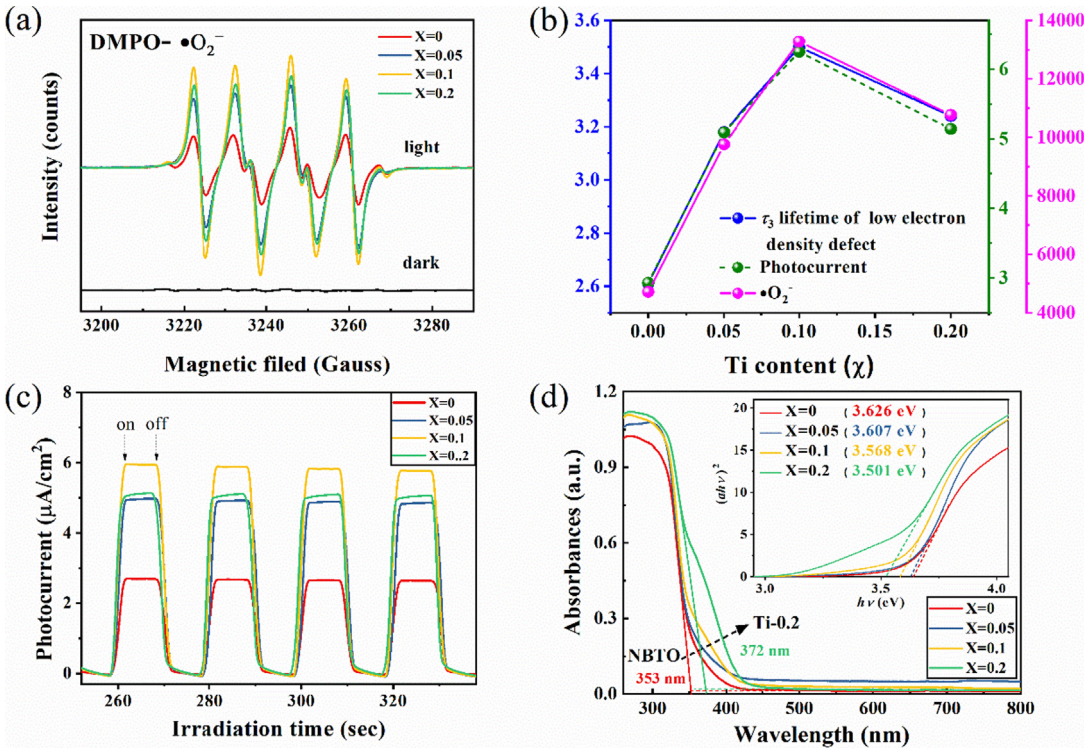

Fig. 4. Physicochemical properties of Ti-*x* samples. (a) ESR detection of $\cdot O_2^-$ using a DMPO spin-trapping agent. (b) Correlation curves between τ_3 positron lifetime and physicochemical properties in Ti-*x* samples. (c) photocurrent-time curves. (d) Optical band gaps of Ti-*x* samples determined by UV − vis diffuse reflectance spectra.

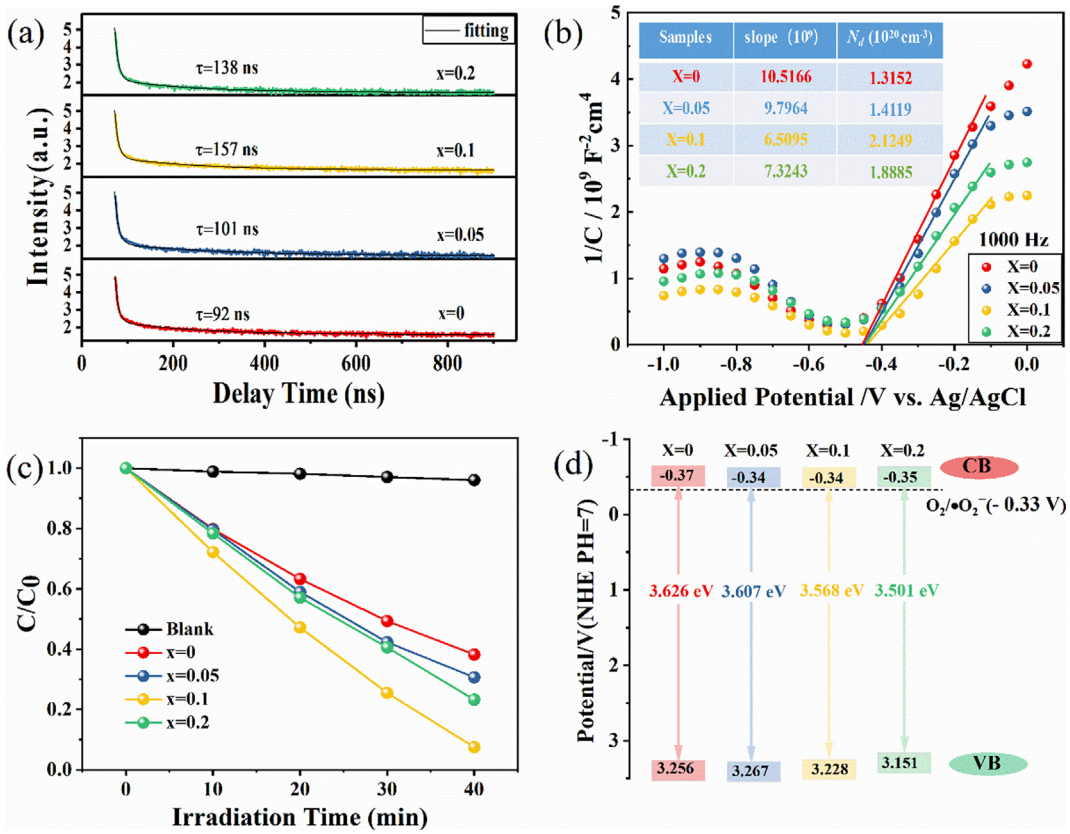

Fig. 5. (a) PL lifetime curves. (b) Mott-Schottky curves of Ti-*x* samples under 1000 Hz and carrier concentration in the insert. (c) Photocatalytic degradation curves of the model substrate (methylene blue) under 20 w UV-lamp irradiation (254 nm). (d) Band position diagram of Ti-*x* samples at pH = 7.

$Na_{0.5}Bi_{2.5}Ta_2O_9$ and 490 nm for Ti-doped samples. The results are depicted in Fig. 5A, and are fitted by the following double-exponential function (Eqs. (3)–(4)) [42].

$$I(t) = A_1 e^{(-t/\tau_1)} + A_2 e^{(-t/\tau_2)} + I(0) \quad (3)$$

The average PL lifetime τ is calculated by the following formula:

$$\tau = (A_1\tau_1^2 + A_2\tau_2^2)/(A_1\tau_1 + A_2\tau_2) \quad (4)$$

PL lifetime increases in the following order: Ti-0 < Ti-0.05 < Ti-0.2 < Ti-0.1, following the change of τ_3. The longer PL lifetime hints the lower carrier recombination rate and the higher photocatalytic activity [42]. This agreement is rational because the PL originates from the recombination of electron and hole trapped at defects, while the component τ_3 reflects the annihilation of electron and positron (*ortho*-positronium) in the large voids. The prolonged lifetime of electron-hole pairs in Ti-0.1 benefits the separation of the pairs, in agreement with the results in Fig. 4B. Subsequently, the Mott-Schottky (MS) and electrochemical impedance spectroscopy (EIS) curves are investigated to evaluate the kinetics of charge transfer properties of Ti-*x* samples. As shown in Fig. 5B, the slopes of all MS curves are positive, indicating Ti-*x* samples are all n-type semiconductor materials. According to the Mott-Schottky equation, the carrier concentrations (N_d) are calculated to be 1.31×10^{20} cm^{-3}, 1.41×10^{20} cm^{-3}, 2.12×10^{20} cm$^{-3,}$ and 1.89×10^{20} cm^{-3}, respectively, which indicates that the carrier density in Ti-0.1 is highest. A higher donor concentration is helpful to enhance conductivity and contribute to higher photocatalytic performance [29,38,43]. The charge transfer at the solid/electrolyte interface can be further determined by the semicircle radius of the EIS curves (Fig. S9). The smaller radius value is, the faster charge transfer is. The radius value of samples decreases in the following order: Ti-0 > Ti-0.05 > Ti-0.2 > Ti-0.1. Previous studies have confirmed that the efficient charge transfer could suppress the charge recombination [43], which will improve the photoelectrochemical performance.

The above results indicate that the decrease of low-electron-density defects will promote the charge separation and transfer and the generation of $\cdot O_2^-$, although the specific nature of this kind of defect is unclear. As a further demonstration and application, the photocatalytic performance is investigated by using MB as a model substrate, and the degradation results are illustrated in Fig. 5C and Fig. S10, the photodegradation rate of MB is about 96.7% with Ti-0.1 catalyst within 40 min under UV-light irradiation, while the degradation rate of that without catalyst only 5%. As expected, the dynamic parameter *k* value and normalized dynamic parameter *k′* (normalized by the BET surface area) of the Ti-0.1 catalyst are the highest (Fig. S11). Also, to further verify the degradation performance, Ti-0.1 shows superior degradation activity and stability of methyl orange (MO) compared to primary $Na_{0.5}Bi_{2.5}Ta_2O_9$ (Fig. S12). What's more, there is no obvious distinction in the XRD patterns and TEM images between before and after the photodegradation experiment (Fig. S13–14).

The above Fig. 4D shows the UV–vis diffuse reflectance spectra of Ti-*x* samples, from which it can be seen that the absorption edges of all samples were around 360 nm. The bandgaps of Ti-*x* samples (x = 0, 0.05, 0.1, and 0.2) are deduced to be 3.63 eV, 3.61 eV, 3.57 eV, and 3.50 eV, respectively. Besides, the Mott-Schottky plots are measured under three frequencies (1 kHz, 3 kHz, 5 kHz), respectively. As shown in Fig. S15, the flat band potential (E_{fb}) of Ti-*x* samples (x = 0, 0.05, 0.1, and 0.2) in Na_2SO_4 solution (pH = 7.0) are −0.47 V, −0.44 V, −0.44 V, −0.45 V versus Ag/AgCl (-0.27, −0.24, −0.24, −0.25 versus NHE), respectively. For n-type conductors, the E_{fb} is usually assumed to be approximately equal to the Fermi level and generally considered to be about 0.1 V lower than the bottom of the conduction band (CB). Derived from above results, the conduction band minimum (CBM) positions of Ti-*x* samples (x = 0, 0.05, 0.1, and 0.2) are approximately −0.37 V, −0.34 V, −0.34 V, and −0.35 V, while the corresponding valence band maximum (VBM) positions are about 3.26 V, 3.27 V, 3.23 V, and 3.15 V, respectively (Fig. 5D). Therefore, the influences of the morphology, specific surface area (Fig. S16), bandgap position, and optical property on physicochemical performance can be excluded because these parameters are very similar in all samples. The correlations between the positron lifetime of low-electron-density defects and physicochemical properties, such as carrier concentration, $\cdot O_2^-$ generation rate, photocurrent, and photocatalytic properties are summarized in Fig. 4B and Table S2. The good correspondence exhibits that the physicochemical properties closely relate with the low-electron-density defects, though the exact nature of this kind of defect is tentatively unknown. From the variation of XPS and XAS, as well as positron lifetime and intensity information of τ_3 of PAS, the defects of component τ_3 may be attributed to a kind of defects with low-electron-density such as nanoscale voids.

Is the correlation between low-electron-density defects and photochemical properties only valid in $Na_{0.5}Bi_{2.5}Ta_{2-x}Ti_xO_{9-\delta}$? To clarify this issue, we have surveyed the data in previous literature, and we find that the physicochemical properties and the low-electron-density defect with τ_3 component in many materials show a rough correlation, which implies that the low-electron-density defect with τ_3 component may also affect the properties of the materials. For example, Kong et al. applied PAS to study photocatalysis in TiO_2 sintered at different temperature and the tendency between τ_3 lifetime and photocatalytic CO_2 variation is similar in Fig. S17 (Fig. 3 in Ref. 7) [7]. Similarly, the relationship between τ_3 lifetime and photocatalytic removal of benzene exhibited in CeO_2–MnO_x composite oxides showed in Fig. S18 (Fig. 1 of Ref. 41), between τ_3 lifetime and photocatalytic CO oxidation efficiency in CeO_2 nanorods performed in Fig. S19 (Fig. 1 of Ref. 8), respectively [8,44]. Yang's group doped cobalt in Li_2FeSiO_4 cathode material for a lithium-ion battery to improve electrochemical performance in Fig. S20 (Fig. 9 of Ref. 42) [45]. Dramatically the electronic conductivity of Co-doped LFS/C and primary LFS/C exhibited a relationship along with τ_3 component. In addition, PAS is a powerful tool to study the defects in ultrathin nanosheets and bulk materials. The trends between properties and τ_3 lifetime of $CoSe_2$ in Fig. S21 (Fig. 3 of Ref. 9) and $WO_3{\cdot}H_2O$ in Fig. S22 (Fig. 2 of Ref. 10) are consistent with the above mentioned phenomena, respectively [9,10]. These correlations appeared in these materials indicate that the low-electron-density defect is important if the process related to low-electron-density defects is the rate-limiting factors, and this kind of defect affects physicochemical properties together with other factors. Therefore, the low-electron-density defect is pervasive for different materials, and it is very important to deeply explore the mechanism of its influence on the physicochemical properties of materials before applying defect engineering.

The high intrinsic electron transfer efficiency and photochemical properties, such as generation rate of $\cdot O_2^-$, photocurrent, and photocatalytic rate after normalization by BET surface area for Ti-0.1 sample can be attributed by the elimination of the low-electron-density defect. The τ_3 component is ascribed to the pick-off annihilation of *ortho*-positronium. In this process, the positron in *ortho*-positronium annihilates with an electron from the surroundings, therefore, the long PAS lifetime indicates the decreased electron–positron annihilation rate. The behavior of positron in a semiconductor can be analogous to that of the hole [46–48]. In other words, the long PAS lifetime may also indicate decreased electron-hole annihilation, which leads to high photocatalytic performance. Summarizing the above results, a possible mechanism of impact of low-electron-density defects on tuning photochemical properties is proposed in Fig. 6. The behavior of recombination of electron and hole trapped at defects is similar to the behavior of the annihilation of electron and positron (*ortho*-positronium) in the large voids. After the separation of electron-hole pairs excited by light, the photogenerated carriers may directly drift partly to the particle surface to trigger the $\cdot O_2^-$ generation, however, the other part may also be trapped and recombine at defects with low-electron-density. The recombination of photogenerated carriers at low-electron-density defect affects the efficiency of the electrons transferred to the surface, and thus is detrimental to the $\cdot O_2^-$ generation and the $\cdot O_2^-$-related photocatalysis

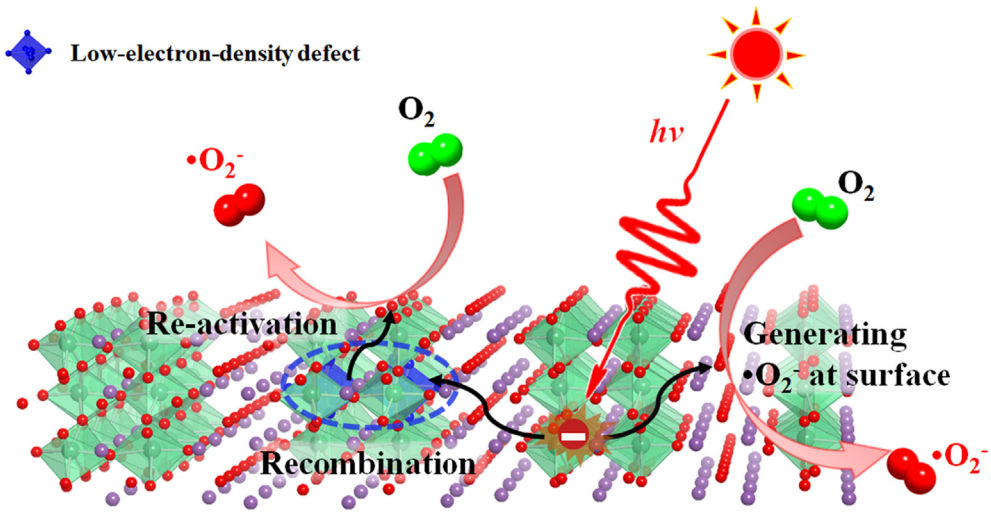

Fig. 6. The schematic of the act of low-electron-density defects on the photochemical process.

reaction. Decreasing the concentration of defects with low-electron-density, together with increasing the lifetime of electron-hole pairs on this kind of defect, will significantly enhance the carrier transfer and the $\cdot O_2^-$ generation, therefore improve the photochemical performance.

4. Conclusions

In summary, it was established for the first time that there are pervasive correlations between the low-electron-density defect and photocatalytic performance. Decreasing the concentration of this kind of defect favors the physicochemical performance in various materials. The findings in this work provide fundamental insight into the function of defects on the physicochemical properties, and are instructive for applying defect-engineering.

Author contributions

Zhengping Fu, Yalin Lu designed this project. Huan Liu conceived and performed experiments. Xiaofeng Yin and Xiaoning Li provided much useful advice and discussion. Huiru Cheng and Bangjiao Ye conducted the positron annihilation measurements. Wen Gu, Yingying Zhang, Liuyang Zhu, and Qingmei Wu conducted XRD, SEM, and TEM measurements. Wei Zou, Haoliang Huang, and Jianlin Wang performed XANES characterization and analyzed some data. Zhengping Fu and Huan Liu wrote the manuscript. All authors commented on the paper.

Declaration of Competing Interest

The authors declare that they have no known competing financial interests or personal relationships that could have appeared to influence the work reported in this paper.

Acknowledgements

This work was financially supported by the National Key Research and Development Program of China (2016YFA0401004), the National Natural Science Foundation of China (51627901), Anhui Initiative in Quantum Information Technologies (AHY100000), Anhui Provincial Natural Science Foundation (1908085ME119) and the Open Programs for the Key Science & Technology Infrastructures of Chinese Academy of Sciences.

Appendix A. Supplementary data

Supplementary data to this article can be found online at https://doi.org/10.1016/j.apsusc.2020.146688.

References

[1] Y. Liu, C. Miao, P. Yang, Y. He, J. Feng, D. Li, Synergetic promotional effect of oxygen vacancy-rich ultrathin TiO_2 and photochemical induced highly dispersed Pt for photoreduction of CO_2 with H_2O, Appl. Catal. B 244 (2019) 919–930.
[2] T.R. Gordon, M. Cargnello, T. Paik, F. Mangolini, R.T. Weber, P. Fornasiero, C.B. Murray, Nonaqueous synthesis of TiO_2 nanocrystals using TiF_4 to engineer morphology, oxygen vacancy concentration, and photocatalytic activity, J. Am. Chem. Soc. 134 (2012) 6751–6761.
[3] H. Yu, J. Li, Y. Zhang, S. Yang, K. Han, F. Dong, T. Ma, H. Huang, Three-in-One oxygen vacancies: whole visible-spectrum absorption, efficient charge separation, and surface site activation for robust CO_2 photoreduction, Angew. Chem. Int. Ed. 58 (2019) 3880–3884.
[4] C.A. Teles, P.M. de Souza, A.H. Braga, R.C. Rabelo-Neto, A. Teran, G. Jacobs, D.E. Resasco, F.B. Noronha, The role of defect sites and oxophilicity of the support on the phenol hydrodeoxygenation reaction, Appl. Catal. B 249 (2019) 292–305.
[5] C. Mao, H. Cheng, H. Tian, H. Li, W.-J. Xiao, H. Xu, J. Zhao, L. Zhang, Visible light driven selective oxidation of amines to imines with BiOCl: Does oxygen vacancy concentration matter? Appl. Catal. B 228 (2018) 87–96.
[6] S. Dutta, S. Chattopadhyay, D. Jana, A. Banerjee, S. Manik, S.K. Pradhan, M. Sutradhar, A. Sarkar, Annealing effect on nano-ZnO powder studied from positron lifetime and optical absorption spectroscopy, J. Appl. Phys. 100 (2006) 114328.
[7] M. Kong, Y. Li, X. Chen, T. Tian, P. Fang, F. Zheng, X. Zhao, Tuning the relative concentration ratio of bulk defects to surface defects in TiO_2 nanocrystals leads to high photocatalytic efficiency, J. Am. Chem. Soc. 133 (2011) 16414–16417.
[8] X. Liu, K. Zhou, L. Wang, B. Wang, Y. Li, Oxygen vacancy clusters promoting reducibility and activity of ceria nanorods, J. Am. Chem. Soc. 131 (2009) 3140–3141.
[9] Y. Liu, H. Cheng, M. Lyu, S. Fan, Q. Liu, W. Zhang, Y. Zhi, C. Wang, C. Xiao, S. Wei, B. Ye, Y. Xie, Low overpotential in vacancy-rich ultrathin $CoSe_2$ nanosheets for water oxidation, J. Am. Chem. Soc. 136 (2014) 15670–15675.
[10] L. Liang, K. Li, C. Xiao, S. Fan, J. Liu, W. Zhang, W. Xu, W. Tong, J. Liao, Y. Zhou, B. Ye, Y. Xie, Vacancy associates-rich ultrathin nanosheets for high performance and flexible nonvolatile memory device, J. Am. Chem. Soc. 137 (2015) 3102–3108.
[11] S. Chakraverty, S. Mitra, K. Mandal, P.M.G. Nambissan, S. Chattopadhyay, Positron annihilation studies of some anomalous features of $NiFe_2O_4$ nanocrystals grown in SiO_2, Phys. Rev. B. 71 (2005) 024115.
[12] S.N. Guin, J. Pan, A. Bhowmik, D. Sanyal, U.V. Waghmare, K. Biswas, Temperature dependent reversible $p-n-p$ type conduction switching with colossal change in thermopower of semiconducting AgCuS, J. Am. Chem. Soc. 136 (2014) 12712–12720.
[13] R.M. de la Cruz, R. Pareja, R. González, L.A. Boatner, Y. Chen, Effect of thermo-chemical reduction on the electrical, optical-absorption, and positron-annihilation characteristics of ZnO crystals, Phys. Rev. B. 45 (1992) 6581–6586.
[14] S. Dannefaer, T. Bretagnon, D. Kerr, Vacancy-type defects in crystalline and amorphous SiO_2, J. Appl. Phys. 74 (1993) 884–890.
[15] D. Sanyal, U. De, K. Mandal, D. Banerjee, R. Bhattacharya, Positronium formation in (Bi/Bi□Pb)-2212 and -2223 superconductors, Phys. Lett. A 204 (1995) 305–309.
[16] D. Sanyal, D. Banerjee, Probing $(Bi_{0.92}Pb_{0.17})_2Sr_{1.91}Ca_{2.03}Cu_{3.06}O_{10+\delta}$ superconductors from 30 to 300 K by positron-lifetime measurements, Phys. Rev. B 58 (1998) 15226–15230.

[17] H. Murakami, N. Onizuka, J. Sasaki, N. Thonghai, Ultra-fine particles of amorphous TiO_2 studied by means of positron annihilation spectroscopy, J. Mater. Sci. 33 (1998) 5811–5814.
[18] T. Ling, D.-Y. Yan, Y. Jiao, H. Wang, Y. Zheng, X. Zheng, J. Mao, X.-W. Du, Z. Hu, M. Jaroniec, S.-Z. Qiao, Engineering surface atomic structure of single-crystal cobalt (II) oxide nanorods for superior electrocatalysis, Nat. Commun. 7 (2016) 12876.
[19] Y. Zhou, Z. Zhang, Z. Fang, M. Qiu, L. Ling, J. Long, L. Chen, Y. Tong, W. Su, Y. Zhang, J.C.S. Wu, J.-M. Basset, X. Wang, G. Yu, Defect engineering of metal–-oxide interface for proximity of photooxidation and photoreduction, Proc. Natl. Acad. Sci. USA 116 (2019) 10232–10237.
[20] S. Zhu, S. Liang, Y. Tong, X. An, J. Long, X. Fu, X. Wang, Photocatalytic reduction of CO2 with H2O to CH4 on Cu(i) supported TiO2 nanosheets with defective 001 facets, Phys. Chem. Chem. Phys. 17 (2015) 9761–9770.
[21] H. Huang, C. Zhou, X. Jiao, H. Yuan, J. Zhao, C. He, J. Hofkens, M.B.J. Roeffaers, J. Long, J.A. Steele, Subsurface defect engineering in single-unit-cell Bi_2WO_6 monolayers boosts solar-driven photocatalytic performance, ACS Catal. 10 (2020) 1439–1443.
[22] P. Zhang, J. Zhang, J. Gong, Tantalum-based semiconductors for solar water splitting, Chem. Soc. Rev. 43 (2014) 4395–4422.
[23] K. Maeda, M. Eguchi, T. Oshima, Perovskite oxide nanosheets with tunable band-edge potentials and high photocatalytic hydrogen-evolution activity, Angew. Chem. Int. Ed. 53 (2014) 13164–13168.
[24] X. Li, H. Liu, Z. Chen, Q. Wu, Z. Yu, M. Yang, X. Wang, Z. Cheng, Z. Fu, Y. Lu, Enhancing oxygen evolution efficiency of multiferroic oxides by spintronic and ferroelectric polarization regulation, Nat. Commun. 10 (2019) 1409.
[25] X. Li, Z. Ju, F. Li, Y. Huang, Y. Xie, Z. Fu, R.J. Knize, Y. Lu, Visible light responsive $Bi_7Fe_3Ti_3O_{21}$ nanoshelf photocatalysts with ferroelectricity and ferromagnetism, J. Mater. Chem. A. 2 (2014) 13366.
[26] X. Yin, X. Li, H. Liu, W. Gu, W. Zou, L. Zhu, Z. Fu, Y. Lu, Realizing selective water splitting hydrogen/oxygen evolution on ferroelectric Bi_3TiNbO_9 nanosheets, Nano Energy 49 (2018) 489–497.
[27] Y. Hu, G. Chen, C. Li, Z. Han, S. Hao, W. Hong, W. Xing, Non-integer induced spontaneous polarization of highly efficient perovskite-based NBTO SCN photocatalysts, J. Mater. Chem. A. 5 (2017) 22984–22987.
[28] E. Boroński, R.M. Nieminen, Electron-positron density-functional theory, Phys. Rev. B. 34 (1986) 3820–3831.
[29] X. Li, W. Gu, F. Wang, X. Yin, L. Zhu, W. Zou, G. Zhang, Z. Fu, Y. Lu, Greatly improved dispersibility of Pt quantum dots in hematite nanoarray and enhanced photoelectrochemical performance, Nanotechnology. 28 (2017) 415603.
[30] M. Matsushita, R. Aoyagi, H. Takeda, S. Okamura, T. Shiosaki, Piezoelectric properties of sodium bismuth tantalate $Na_{0.5}Bi_{2.5}Ta_2O_9$ dense ceramics, Jpn. J. Appl. Phys. 43 (2004) 7164–7168.
[31] W. Yan, Z. Sun, Z. Pan, Q. Liu, T. Yao, Z. Wu, C. Song, F. Zeng, Y. Xie, T. Hu, S. Wei, Oxygen vacancy effect on room-temperature ferromagnetism of rutile Co:TiO_2 thin films, Appl. Phys. Lett. 94 (2009) 042508.
[32] W. Wang, Y. Ye, J. Feng, M. Chi, J. Guo, Y. Yin, Enhanced photoreversible color switching of redox dyes catalyzed by barium-doped TiO_2 nanocrystals, Angew. Chem. 127 (2015) 1337–1342.
[33] J. Jeong, N. Aetukuri, T. Graf, T.D. Schladt, M.G. Samant, S.S.P. Parkin, Suppression of metal-insulator transition in VO_2 by electric field-induced oxygen vacancy formation, Science 339 (2013) 1402–1405.
[34] Z. Cui, H. Xu, Y. Yun, J. Guo, Y.-D. Chuang, H. Huang, D. Meng, J. Wang, Z. Fu, R. Peng, R.J. Knize, G.J. Brown, X. Zhai, Y. Lu, Soft X-ray absorption spectroscopy investigations of $Bi_6FeCoTi_3O_{18}$ and $LaBi_5FeCoTi_3O_{18}$ epitaxial thin films, J. Appl. Phys. 120 (2016) 084101.
[35] S. Wang, P. Chen, Y. Bai, J.-H. Yun, G. Liu, L. Wang, New $BiVO_4$ dual photoanodes with enriched oxygen vacancies for efficient solar-driven water splitting, Adv. Mater. 30 (2018) 1800486.
[36] X. Zhang, J. Qin, Y. Xue, P. Yu, B. Zhang, L. Wang, R. Liu, Effect of aspect ratio and surface defects on the photocatalytic activity of ZnO nanorods, Sci Rep. 4 (2015) 4596.
[37] K.-N. Jung, J.-H. Jung, W.B. Im, S. Yoon, K.-H. Shin, J.-W. Lee, Doped lanthanum nickelates with a layered perovskite structure as bifunctional cathode catalysts for rechargeable metal-air batteries, ACS Appl. Mater. Interfaces 5 (2013) 9902–9907.
[38] S. Yu, Y. Zhang, F. Dong, M. Li, T. Zhang, H. Huang, Readily achieving concentration-tunable oxygen vacancies in $Bi_2O_2CO_3$: Triple-functional role for efficient visible-light photocatalytic redox performance, Appl. Catal. B 226 (2018) 441–450.
[39] J. Meng, Q. Lin, T. Chen, X. Wei, J. Li, Z. Zhang, Oxygen vacancy regulation on tungsten oxides with specific exposed facets for enhanced visible-light-driven photocatalytic oxidation, Nanoscale. 10 (2018) 2908–2915.
[40] H. Huang, S. Tu, C. Zeng, T. Zhang, A.H. Reshak, Y. Zhang, Macroscopic polarization enhancement promoting photo- and piezoelectric-induced charge separation and molecular oxygen activation, Angew. Chem. Int. Ed. 56 (2017) 11860–11864.
[41] P. Klason, T. Moe Børseth, Q.X. Zhao, B.G. Svensson, A.Yu. Kuznetsov, P.J. Bergman, M. Willander, Temperature dependence and decay times of zinc and oxygen vacancy related photoluminescence bands in zinc oxide, Solid State Commun. 145 (2008) 321–326.
[42] X. Yin, X. Li, W. Gu, F. Wang, Y. Zou, S. Sun, Z. Fu, Y. Lu, Enhanced photocatalytic activities of g-C_3N_4 via hybridization with a Bi–Fe–Nb-containing ferroelectric pyrochlore, ACS Appl. Mater. Interfaces 9 (2017) 19908–19916.
[43] M. Ma, K. Zhang, P. Li, M.S. Jung, M.J. Jeong, J.H. Park, Dual oxygen and Tungsten vacancies on a WO_3 photoanode for enhanced water oxidation, Angew. Chem. 128 (2016) 11998–12002.
[44] Z. Wang, G. Shen, J. Li, H. Liu, Q. Wang, Y. Chen, Catalytic removal of benzene over CeO_2–MnOx composite oxides prepared by hydrothermal method, Appl. Catal. B 138–139 (2013) 253–259.
[45] L.-L. Zhang, S. Duan, X.-L. Yang, G. Liang, Y.-H. Huang, X.-Z. Cao, J. Yang, M. Li, M.C. Croft, C. Lewis, Insight into cobalt-doping in Li_2FeSiO_4 cathode material for lithium-ion battery, J. Power Sources 274 (2015) 194–202.
[46] I. Makkonen, M.J. Puska, Energetics of positron states trapped at vacancies in solids, Phys. Rev. B. 76 (2007) 054119.
[47] A.A. Belyanin, V.V. Kocharovsky, V.V. Kocharovsky, Cooperative coherent phenomena in annihilating electron-positron and electron-hole plasmas in a strong magnetic field, Computers Math. Applic. 34 (1997) 845–880.
[48] G. Alymov, V. Vyurkov, V. Ryzhii, A. Satou, D. Svintsov, Auger recombination in Dirac materials: a tangle of many-body effects, Phys. Rev. B. 97 (2018) 205411.